Ionized gas kinematics of cluster AGN at z ∼ 0.8 with KMOS

Marcela Paillalef, Hector Flores, Ricardo Demarco, Alessando Rettura, Yara Jaffé, Chris Lidman, Julie Nantais, Mathieu Puech, Piero Rosati

Monthly Notices
of the
ROYAL ASTRONOMICAL SOCIETY

MNRAS **506,** 385–395 (2021)
Advance Access publication 2021 June 16

https://doi.org/10.1093/mnras/stab1731

Ionized gas kinematics of cluster AGN at z ∼ 0.8 with KMOS

Marcela G. Paillalef,[1★] Hector Flores,[2★] Ricardo Demarco,[1★] Alessando Rettura,[3] Yara Jaffé,[4] Chris Lidman,[5,6] Julie Nantais,[7] Mathieu Puech[2] and Piero Rosati[8]

[1]*Departamento de Astronomóa, Universidad de Concepción, Casilla 160-C, 4030000 Concepción, Chile*
[2]*GEPI - Observatoire de Paris Meudon. 5 Place Jules Jannsen, F-92195 Meudon, France*
[3]*Jet Propulsion Laboratory, Cahill Center for Astronomy & Astrophysics California Institute of Technology, 4800 Oak Grove Drive, Pasadena, 91109 CA, USA*
[4]*Instituto de Física y Astronomía, Universidad de Valparaíso, Gran Bretana 1111, Valparaíso, Chile*
[5]*Research School of Astronomy and Astrophysics, The Australian National University, ACT 2601, Australia*
[6]*Centre for Gravitational Astrophysics, College of Science, The Australian National University, ACT 2601, Australia*
[7]*Departamento de Ciencias Físicas, Universidad Andrés Bello, Fernandez Concha 700, Las Condes 7591538, RM, Chile*
[8]*Dipartimento di Fisica e Scienze della Terra, Università degli Studi di Ferrara, via Saragat 1, I-44122 Ferrara, Italy*

Accepted 2021 June 10. Received 2021 May 18; in original form 2021 January 12

ABSTRACT

We present an integral field spectroscopy study of two active galactic nuclei (AGN) in the galaxy cluster RXJ0152–137 at z = 0.84. We have combined integrated and 3D spectra with *HST* images to perform a complete morpho-kinematical analysis of each galaxy. For G557, we detect narrow and broad H α and [N II] emission. The broad H α component is redshifted by v ∼ 939 km s^{-1} concerning the narrow component. The kinematics analysis and VLT/FORS2 data indicate that G557 presents evidence of radial outflows. For G300, it was possible to detect only the broad H α emission. The spectral properties of both galaxies are equivalent to those of local AGN. We also compare the results obtained for each AGN with their location within the cluster. We found a possible connection of the environment with the properties inferred for each of them, and the possible interaction of G557 with an unconfirmed neighboring galaxy, for which a bridge-like structure is observed in the *HST* images. This work shows evidence of how the same type of AGN can show differences in their spectroscopic properties depending on the region of the cluster in which they develop, which is important to understand how the environment affects AGN and, consequently, the evolution of galaxies.

Key words: galaxies: active – galaxies: high-redshift – galaxies: kinematics and dynamics.

1 INTRODUCTION

There is evidence of co-evolution between the growth of super massive black holes (SMBHs) and the star formation in galaxies (Alexander & Hickox 2012; Kormendy & Ho 2013). For example, one of the most direct results of this connection is that active galactic nuclei (AGN) activity and the star formation rate in galaxies show a similar cosmic evolution from z ∼ 2 to the present (Franceschini et al. 1999; Kauffmann et al. 2003; Merloni, Rudnick & Di Matteo 2004; Madau & Dickinson 2014; Aird et al. 2015). Any mechanism that enables the input of cold gas in a galaxy has the potential to trigger star formation as well as AGN activity. Then, it is thought that AGN feedback can regulate star formation, stripping the galaxy off of its cold gas or heating its interstellar medium (ISM; Fabian 2012; Somerville & Davé 2015), for which it is assumed that AGNs are a phase of galaxy evolution. Therefore, studying AGNs can contribute to understanding the evolution of galaxies.

Galaxies are not isolated in the Universe. In that context, they can interact with objects and surrounding matter depending on the environment in which they develop. The best laboratories to study how the environment can influence the features of AGNs are galaxy clusters. The processes that shape galaxy properties are expected to be more important in this type of environment due to the larger density of the intracluster medium (ICM), galaxies, and dark matter (Overzier 2016).

Galaxies in clusters are known to evolve faster than galaxies in low density environments (Rettura et al. 2011). This is evidenced by the significantly larger fraction of red elliptical galaxies than in the field, known as the morphology–density relation (Dressler 1980; Postman & Geller 1984; Postman et al. 2005; Holden et al. 2007; van der Wel et al. 2007; Mei et al. 2012; Bassett et al. 2013; Houghton 2015), and the fraction of star-forming cluster galaxies that increases strongly with redshift and also with ratio (Butcher & Oemler 1984; Ellingson et al. 2001).

Studies have shown that AGN are less frequent in cluster environments than in low-density areas such as the field (Dressler, Thompson & Shectman 1985; Ehlert et al. 2014) but, the fraction of AGN seems to increase toward low clustercentric radii (Galametz et al. 2009; Martini et al. 2013). Also, a clear dependence on redshift is reported where the frequency of AGN in galaxy clusters increases with increasing redshift (Galametz et al. 2009; Martini et al. 2013; Pentericci et al. 2013; Bufanda et al. 2016). This is interpreted as evidence that the AGN population in clusters has evolved faster than the field population from at least z ∼ 1.5 to the present (see Martini et al. 2013).

★ E-mail: marcegonzalezp@udec.cl (MGP); hector.flores@obspm.fr (HF); rdemarco@astro-udec.cl (RD)

There is convincing evidence that galaxy mergers and interactions play an important role in the triggering and evolution of AGN where the prevailing theoretical framework is that the most luminous AGN and starbursts are triggered by major mergers of gas-rich galaxies (Barnes & Hernquist 1991; Hopkins et al. 2006, 2008; Treister et al. 2010, 2012). Also, there is evidence that obscured AGN inhabit denser environments than unobscured AGN (Donoso et al. 2014). In a cluster environment, additional mechanisms may interfere with the transport of cold gas that serves as the main fuel for the central black hole. These processes include the removal of the cold gas by the ram-pressure stripping process (Gunn & Gott 1972; Sheen et al. 2017), evaporation of the gas due to the high temperature in the ISM (Cowie & Songaila 1977), tidal effects due to the cluster potential (Farouki & Shapiro 1981; Merritt 1983; Gnedin 2003) and other galaxies (Richstone 1976; Moore et al. 1996), and a lack of gas due to the absence of new cold gas infiltration (Larson, Tinsley & Caldwell 1980). On the other hand, Poggianti et al. (2017) suggest that the mechanism of ram-pressure stripping may act as a trigger of for the activity of an AGN by causing gas to flow towards the centre of the galaxy. Therefore, the physical mechanisms that contribute to the triggering or suppression of the AGN activity are still a matter of debate, especially at high redshift where the fraction of clusters decreases and the analysis of these processes in this type of environment becomes more complex.

Currently, integral field spectroscopy (IFS) offers us the possibility of spatially resolving the distribution of gas and stars in galaxies as well as their internal kinematics. IFS studies with the first generation of instruments such as SINFONI (Eisenhauer et al. 2003) at the *Very Large Telescope* (*VLT*) and OSIRIS (Larkin et al. 2006) at the W. M. Keck Observatory have been very relevant to understand the internal processes that trigger the early growth of massive galaxies (Förster Schreiber et al. 2006, 2009, 2018; Genzel et al. 2006; Shapiro et al. 2008; Jones et al. 2013; Davies et al. 2019). Regarding the study of AGN, IFS through SINFONI and the new second generation of instruments such as the Multi-Unit Spectroscopic Explorer (MUSE; Bacon et al. 2010) in the optical spectral range, and the K-band Multi Object Spectrograph (KMOS; Sharples et al. 2004; Sharples et al. 2013) in the near-infrared bands has promoted a great advance in the analysis of these objects since it has allowed to spatially solve the structure, extension, and kinematic of AGN outflows (Riffel, Storchi-Bergmann & Winge 2013; Collet et al. 2016; Harrison et al. 2016; Radovich et al. 2019; Davies et al. 2020). With these new advanced instruments it is now possible to efficiently obtain large samples of near-infrared IFS data where, for example, KMOS is ideal for systematic studies of the rest-frame optical properties of high-redshift galaxies and AGN (Wisnioski et al. 2015, 2019; Harrison et al. 2016, 2017; Stott et al. 2016).

Rodrigues et al. (2016) studied a representative sample of intermediate-mass galaxies at $z \sim 1$ from the KMOS^{3D} survey (Wisnioski et al. 2015, 2019) in order to define a methodology that can robustly identify virialized and isolated discs of galaxies involved in a merging sequence. They combined kinematic results with morphological analyses of *HST* images to define a complete morpho-kinematic classification of these galaxies.

In this paper, we present the integral field spectroscopy analysis of two cluster AGN at $z \sim 0.8$ using observations from the KMOS instrument. We complemented these results with photometric analysis of *HST*/ACS images in order to uncover signs of processes that may affect their internal kinematics and morphology as a consequence of the cluster environment.

The organization of the paper is as follows. In Section 2 we present the observational details and the method with which we reduced the data. In Section 3 we present the methods of analysis and the preliminary results for each individual target, separating this section into the description of integrated spectrum analysis, kinetic mapping, morpho-kinematic analysis, and emission line distribution analysis. Then, we summarize the main results found for each AGN in Section 4, whereas in Section 5 we discuss the differences found between them and a possible connection with the cluster environment. Finally, we summarize this work in Section 6. Throughout this manuscript, we adopt $H_0 = 70\,km\,s^{-1}\,Mpc^{-1}$, $\Omega_M = 0.3$, and $\Omega_\Lambda = 0.7$.

2 OBSERVATION AND DATA REDUCTION

We used integral field spectroscopy data of two AGN in the galaxy cluster RXJ0152–137 at $z = 0.84$ (Demarco et al. 2005, 2010) observed with KMOS at the *VLT*. These sources correspond to Galaxy ID = 557 (G557) and Galaxy ID = 300 (G300), at redshifts $z = 0.8672$ and $z = 0.8201$, respectively (Demarco et al. 2005).

The observations are part of four observational programs (PI R. Demarco) between the years 2013 and 2016. These are the ESO programs ID = 092.A-0868, 093.A-0834, 096.A-0171, and 098.A-0380. We observed a total of 131 galaxies in six different galaxy clusters, including the two AGNs used in this study. In all programs the data were obtained in the nod-to-sky mode with an object-sky observation sequence of AB AB, that is, one sky observation for each object observation.

The observations of both AGN included five nights dated 2013-10-02, 2014-12-21, 2015-10-30, and 2016-10-12, collecting a total of 39 exposures with an exposure time of 600 s for science objects. Both sources were observed in the YJ band that has a spectral coverage of 1.01–1.35 μm and a typical resolving power of $R \sim 3600$ under seeing conditions of 0.7–0.8 arcsec, in the optical range.

Data reduction was done using The Software Package for Astronomical Reductions with KMOS (SPARK; Davies, Agudo Berbel & Wiezorrek 2013), a command-line set made to reduce KMOS/*VLT* data. The sky subtraction was performed selecting theSKYTWEAK optional routine within the ESOREX pipeline. This method makes an enhanced OH line removal, via spectral scaling of the individual OH line families to match the data (Davies 2007). In addition, to obtain the final cubes for each AGN we combined all the individual observations performed in order to increase the signal-to-noise from the data. Then, a visual inspection of the data cubes was performed and a mask was applied to clean the science spectra from skyline residuals in each spatial pixel before the line profile fitting. For each galaxy we have *HST* images and produced a mask of bad pixels. The details of the observation and data reduction of the *HST* images are explained in Blakeslee et al. (2006). These data have also been used and described in Postman et al. (2005), Demarco et al. (2010), and Nantais et al. (2013). Finally, we performed a spectral cut from 1.18 μm to 1.26 μm for G557, and from 1.14 μm to 1.23 μm for G300 to limit the spectrum to the range of emission line detection wavelengths.

3 DATA ANALYSIS

3.1 Emission line fitting

We fitted and subtracted the continuum emission from the reduced data cubes by measuring the continuum level from two emission line-free windows around the detected emission in the integrated spectrum using the LMFIT package. Then, we applied the method

Table 1. Emission lines parameters for each source.

Source	Line	λ_0 [Å]	λ_{obs} [Å]	FWHM [km s^{-1}]	FLUX [10^{-17} erg s^{-1} cm^{-2}]	Reduced χ^2
ID = 557	[N II]	6548	12 230 ± 1	694 ± 90	2.52 ± 0.50	0.007521
	H α_{narrow}	6563	12 254 ± 1	571 ± 66	5.88 ± 1.17	
	H α_{broad}	6563	12 293 ± 2	4,572 ± 179	63.33 ± 12.67	
	[N II]	6584	12 296 ± 1	690 ± 90	7.58 ± 1.51	
ID = 300	H α_{broad}	6563	11 956 ± 1	3,865 ± 101	44.42 ± 8.89	0.002873

to all spaxels of the cube with the SPECTRAL_CUBE package from PYTHON (Astropy Collaboration 2013, 2018).

To perform the fitting to each spaxel we first carry out a general inspection of the integrated spectra in the central region of the data cube to know the type of fitting required. After a visual inspection of the residues and the emission profile of some spaxels, we determined to perform a multiple Gaussian fitting, one Gaussian for each emission line detected.

For each spectrum we test a two-Gaussian component fitting for the H α emission line, with one narrow and one broad component. Besides, we fit two other Gaussian profiles to each line of the [N II] doublet, considering a relation between them that is equal to the theoretical relation of 1:3 (Osterbrock & Ferland 2006), together with a same value in dispersion since they correspond to lines that must come from the same region of the Galaxy. For the case of the narrow line emission of H α and [N II], we tested two possibilities, a fit in which all the narrow components have the same width and another in which their widths are different. Also, we set the condition of signal-to-noise ratio (S/N) > 5 for line detection, according to the simulations performed by (Yang et al. 2008). Finally to choose the best of the two possibilities, we selected the fit with the lowest value of χ^2.

On the other hand, when fitting the broad component of H α we assumed in the first instance that it should be centred at the same central wavelength of its narrow component. However, as described below, for the case of G557 this does not correspond to the best fit. The parameters found with the best fit for each emission line in both AGN are presented in the Table 1.

3.1.1 *AGN G557 emission profiles*

For this Galaxy the narrow emission lines of H α and [N II] were detected as well as a broad component for H α, which is redshifted with respect to the centre of the narrow line as shown in Fig. 1. We measure a z = 0.8730 ± 0.0005 and a redshifted velocity of v = 938 ± 74 km s^{-1} for that component.

This type of AGN spectrum was also found in low redshift AGN (z < 0.37) by Zhang et al. (2009) in a sample of galaxies selected from the SDSS DR4 (Adelman-McCarthy et al. 2006). In their paper they propose a model where the appearance of a broad blue/red-shifted component in low ionization lines such as H α can be explained as the partial obscuration of the broad line region (BLR) in an AGN with double-peaked low ionization broad emission lines, also called dbp-emitters.

3.1.2 *AGN G300 emission profiles*

For this Galaxy the same procedure of multi-Gaussian fitting was adopted in a first instance. However, the narrow lines for H α and [N II] were not detected since none of the fits satisfied the S/N > 5 detection criterion. Therefore, as it is shown in Fig. 1, only the emission corresponding to the broad component of H α was observed which, unlike G557, is centred on the wavelength where the narrow H α emission would be expected. Torres-Papaqui et al. (2020) performed a statistical analysis of 3896 Seyfert 1 (Sy1) galaxies detected with WISE at z < 0.4. They found that 36 per cent of the sample presented only broad components for Balmer lines.

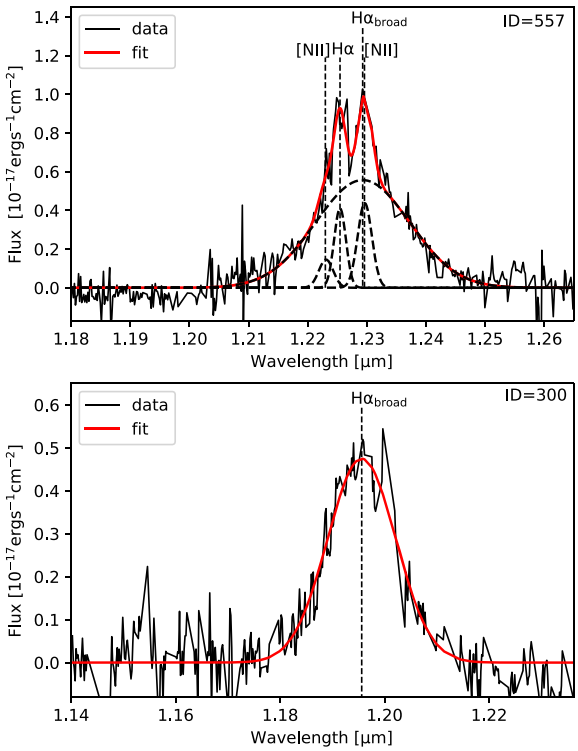

Figure 1. Integrated spectrum of both AGN from the galaxy cluster RXJ0152–137 at z = 0.84 obtained with the KMOS instrument at the *VLT*. Top frame: Integrated spectrum of G557. The black curves show the Gaussian components fitted to each emission line. The thin vertical black dashed lines indicate their centres. A redshifted broad component of H α (H α_{broad}) is detected, with a redshifted velocity of v = 938 ± 74 km s^{-1}. Bottom frame: Integrated spectrum of G300. For this Galaxy it was possible to detect only the broad component of H α. The black dashed line shows the wavelength position where the emission line was detected. In both frames, the red solid curve shows the best multi-Gaussian fit found for these galaxies using the PYTHON LMFIT package.

3.2 Kinematical mapping

We fitted the emission line profile following the methodology described in Section 3.1 for each spaxel of the data cubes to measure the flux, central wavelength, and dispersion parameters for each

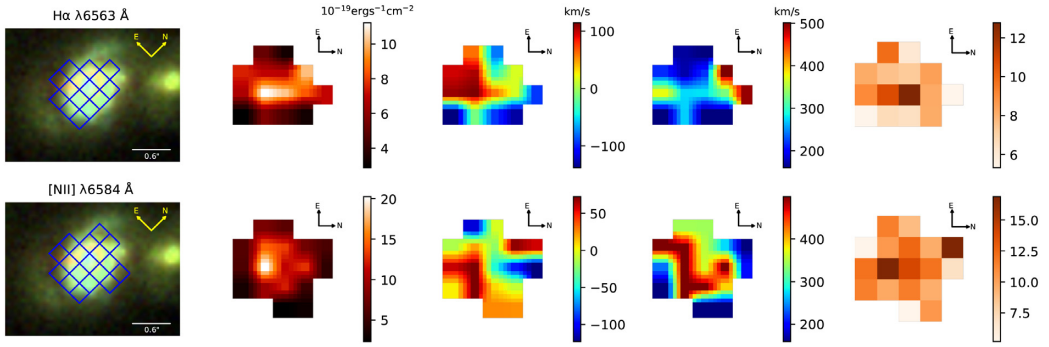

Figure 2. Kinematic characterization of G557 in the cluster RXJ0152–137 at z = 0.84 from the H α and [N II] emission lines detected with KMOS instrument on the *VLT*. From left to right: the *HST* colour image and the spatial footprint covered by the KMOS spaxels with S/N > 5 (blue boxes), flux distribution, the velocity fields, velocity dispersion maps, and the S/N maps for each detected emission feature. The solid white line in the colour image represents the estimated value of the Point Spread Function (PSF) diameter (∼6 arcsec) for the KMOS data. For visualization purposes, each spatial pixel in velocity and dispersion has been linearly interpolated 5 × 5. At first view, this Galaxy present a disturbed kinematics.

emission line in order to construct the flux distribution maps, velocity, and velocity dispersion maps. We estimated the S/N of each line using the method described by Flores et al. (2006). However, for the case of G557 we extend the method to a multi-Gaussian fitting. To measure the noise, we simply calculate the dispersion of the data in emission line-free windows, one on each side of the H α and [N II] emission, in the same region where we had previously fitted the level of the continuum.

The KMOS field of view is split into 196 spaxels in total, from which only 18 of them satisfy the restriction in S/N > 5 for G557. In the case of the AGN with multiple emission lines, even though both [N II] lines were detected, we cannot find spaxels with a S/N > 5 for [N II]λ6548. Therefore, only [N II]λ6583 was considered for the kinematic analysis.

On the other hand, the KMOS data present a full width at half-maximum (FWHM) of the seeing disc of ∼0.6 arcsec that does not allow us to spatially resolve the broad emission lines. The size of the BLR is less than 100 pc (Peterson 1997). Therefore, the emission from this region can be considered as that of a point source. The BLR has only recently been resolved through the implementation of latest generation instruments such as GRAVITY at the *VLT* (Gravity Collaboration 2020a, b). Consequently, in this work we cannot consider the broad emission lines to construct velocity and flux distribution maps. Therefore, the kinematic analysis was performed only on G557, which we have a detection of narrow emission lines for.

We corrected the observed FWHM for instrumental resolution, $FWHM_{ins}$, by using the FWHM of sky lines that corresponds to a value of ∼0.00035 μm. Finally, for G557, we constructed a set of four maps (see Fig. 2): flux distribution, velocity field, velocity dispersion map, and S/N map. For visualization purposes, each KMOS spatial pixel has been simply interpolated using a 5 × 5 box. Visually, from Fig. 2, we observe that G577 does not show a rotational disc signature. However, to know the orientation of the gas movement and then associate this perturbation with a possible interaction process, we measured the kinematic position angle using the method described by (Rodrigues et al. 2016). For this, we first look for the maximum and minimum of the velocity values in each velocity map, where we define as peaks the values that are ∼2 times greater than the average velocity. Then, the kinematic position angle (PA_{kin}) was defined as the angle of the axis that connect the position of the maximum and minimum values with respect to north of photometric images.

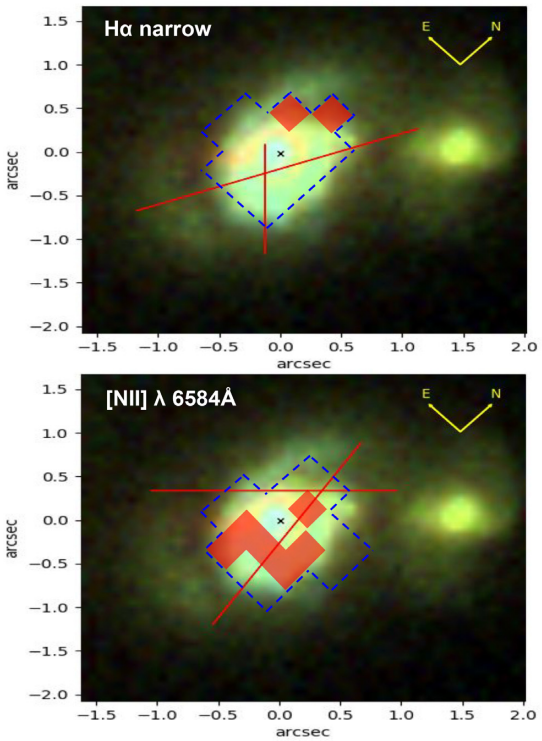

Figure 3. Measurement of the dispersion peak positions for G557. Figure shows the colour image of the Galaxy obtained with the *HST* in the F625W, F775W, and F850LP bands. The blue dashed contours show the detection area of each emission line. The kinematic axes found in each velocity map are shown by the solid red lines. In each image, the dispersion peaks are indicated with red squares of size equivalent to the spaxel which they were detected in. It is clear that this AGN shows a disturbed kinematics since it presents two kinematic axes and the dispersion peaks do not coincide with the photometric centre of the Galaxy (black cross) found in Section 3.3.

On the other hand, using the velocity dispersion maps, we also calculate the peaks in dispersion defined as the spaxels whose dispersion value is ∼1.5 times the average of the whole map.

We found two kinematic axes for each narrow emission line detected in G557 and two or more velocity dispersion peaks.

In Fig. 3 we present the colour image of G557 obtained from the F625W, F775W, and F850LP *HST* bands with the dispersion

Table 2. Parameters of the outermost ellipse fitted with the IRAF ELLIPSE task for each AGN.

ID	SMA [kpc]	ELLIP	PA [deg]	F850LP MAG
557	7.79	0.33 ± 0.01	60.41 ± 0.96	19.54 ± 0.01
300	7.08	0.44 ± 0.01	89.05 ± 1.58	19.64 ± 0.02

peak positions denoted by red boxes. The kinematic axis measured for each detected emission line is shown with solid red lines. We observed that in both cases the velocity dispersion peaks are shifted with respect to the photometric centre of the Galaxy measured in the analysis performed in Section 3.3. Consequently, at first sight, this Galaxy has a perturbed kinematics.

3.3 Photometric analysis

In order to measure the photometric position angle (PA_{phot}), we performed a photometric analysis for both AGN using the *HST* ACS/WFC imaging data in the broad-band filter F850LP. We used the ELLIPSE IRAF task to fit elliptical isophotes on the images to characterize the surface brightness distribution. To begin the fitting, we first mask and remove the neighbouring galaxies to both AGN present in the images, in order to fit only the flux from the galaxies under study. We carry out the fitting in INTERACTIVE mode to visualize in ds9 the fitted isophotes. We checked that the outer isophote is 1σ above the background level. We consider the position angle (PA) defined by this last isophote as PA_{phot}. Table 2 shows the fitted parameters for each source.

3.3.1 Bar detection

It is well known that bars drive the secular evolution of galaxies, that is, a relatively slow evolution resulting from the movement of material through the bar (Combes & Sanders 1981; Weinberg 1985; Weinberg & Katz 2007). The bars are efficient in conducting the gas towards the centre of the galaxy (see Sakamoto et al. 1999). This is due to a loss of angular momentum as bars are known to be efficient at transferring angular momentum from the centre out. This can also change the orbits of the stars, thus giving bars a possible role in the formation of the bulge.

We used the fitted parameters to detect the presence of a bar that was recognized by the variations of the values of ellipticity and PA. It is expected to find an increase in ellipticity until it reaches a maximum value (greater than 0.25) and then begin to decline by at least 0.1, while the PA values remain constant (within 10°), and then change at the transition point between the bar and the disc (Sheth et al. 2003; Marinova & Jogee 2007; Barazza, Jogee & Marinova 2008). In the case of the presence of spiral arms, the variations of these parameters are more complex where the ellipticity can oscillate and the PA can change value abruptly (Barazza et al. 2008).

For G300 we observe in Fig. 4 that, starting from a radius of ∼ 1.82 kpc outward, the ellipticity begins to increase until it reaches a maximum value of 0.45 and then decreases to values of ∼ 0.35. Also, in the same interval, the PA remains constant. With these two results, it is evident the presence of an internal structure in the form of a bar observable from ∼ 1.82 kpc to ∼ 7 kpc due to the PSF of the images, which corresponds to a value of 2 pixels (Nantais et al. 2013).

We will consider the PA of the bar (PA_{bar}) as the average of all the PA values of the isophotes fitted between the radii where the bar is observable, and whose value is ∼ 68.49°. Fig. 5 shows the colour

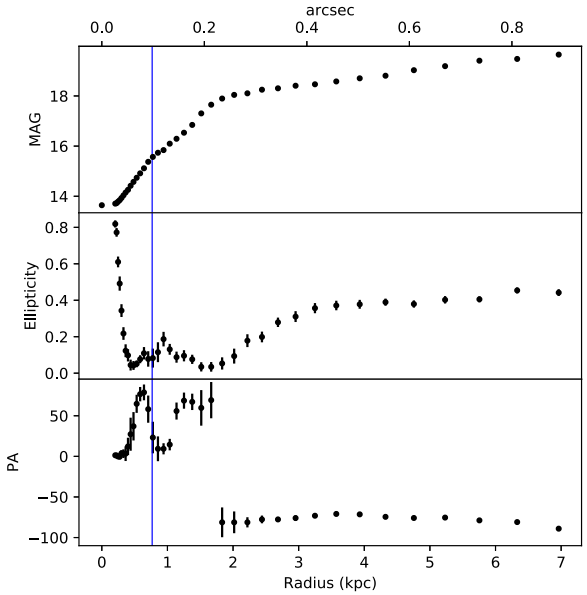

Figure 4. Radial variation of the measured parameters from the fitting of elliptical isophotes with the IRAF ELLIPSE task for G300. From top to bottom: The magnitude, ellipticity, and PA of each ellipse as a function of radius in kpc and arcsec (secondary x-axis). The blue solid line denotes the FWHM of the PSF in the F850LP band, which corresponds to a value of ∼ 2 pixels (∼ 0.1 arcsec) corresponding to ∼ 0.78 kpc at z = 0.8672. We observe that from a radius of ∼ 1.82 kpc there is evidence of the presence of a bar since the ellipticity gradually increases to a value of 0.45 and the PA remains constant.

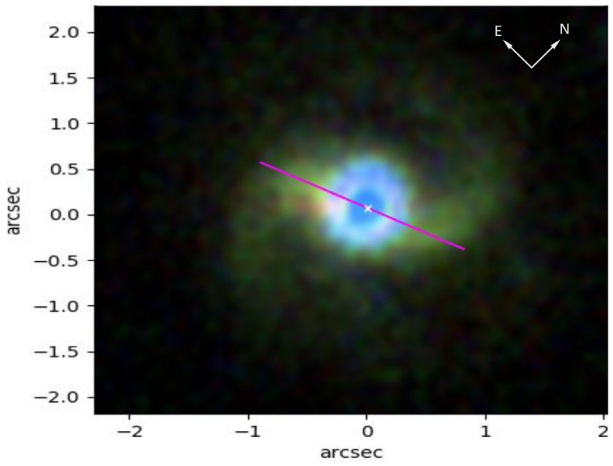

Figure 5. The colour image of G300 obtained from *HST* images in the F625W, F775W, and F850LP bands. The pink solid line represents the bar detected using the elliptical isophotes fitting. Visually, this Galaxy shows a regular morphology. However, due to the blueness of its centre it has been classified as Pec/AGN by Nantais et al. (2013).

image of G300 with the position of this bar in pink colour. Since a spatial analysis of the gas kinematics cannot be performed, we are not able to directly compare the position of the bar with the movement of the ionized gas. Therefore, in this analysis, it is not possible to check for the existence of clear evidence of the bar influence on the AGN activity of this Galaxy. However, we may say that it is known that bars are structures that efficiently transfer angular momentum from the inside out (e.g. Petersen, Weinberg & Katz 2019), making possible the fall of gas into the galaxy core, thus feeding the central SMBH.

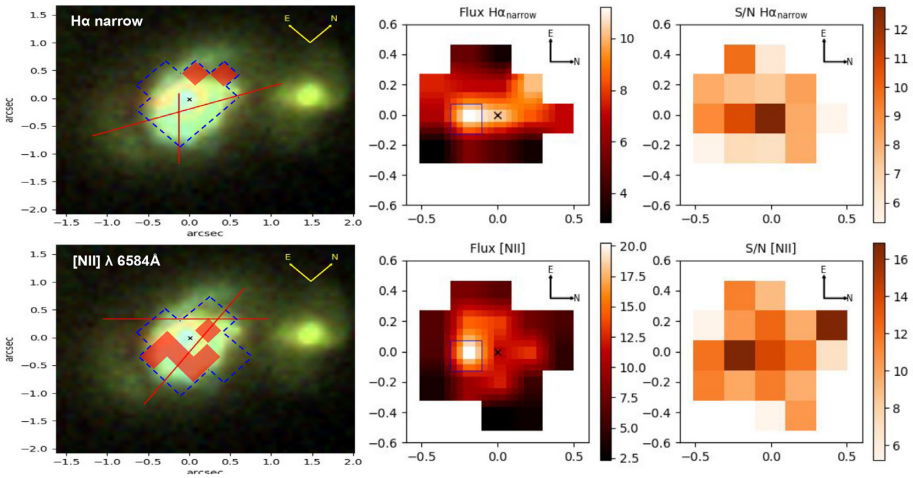

Figure 6. Integrated flux maps of the narrow emission lines detected in the G557. The black cross indicates the photometric centre of the Galaxy found in Section 3.3. The blue squares indicate the position of the spaxel where the emission peaks of each line were detected. The peaks for H α_{narrow} and [N II] emission come from the same spaxel whose centre is offset by 0.2 arcsec from the photometric centre, equivalent to $\sim$ 1.56 kpc of distance at z = 0.8672. For visualization purposes, each original KMOS spaxel has been linearly interpolated into 5 × 5 squares on the flux maps.

In the case of G557, it was not possible, with this method, to distinguish the presence of a bar.

3.4 Morpho-kinematic Classification

Nantais et al. (2013) show the morphological analysis of 124 spectroscopically confirmed members of the cluster RXJ0152–1357 among which our sources are. In that work, for the morphological classification they included colour information, visual morphology, and a light profile fitting of galaxies with 1 or 2 components using the software GALFIT (Peng et al. 2002) on *riz HST* images following the classification criteria described by Neichel et al. (2008) and Delgado-Serrano et al. (2010). This analysis gave a Pec/M classification for the G557, that is, a peculiar morphology (unusually shaped galaxy) with signs of a merger due to the blueness of its centre and the possible interaction with its neighbor on the north-west that is clearly seen in the photometric images (see Fig. 3). On the other hand, a Pec/AGN classification was given to G300, that is, peculiar morphology with sign of AGN activity, also because its centre is considerably bluer than the rest of the Galaxy (see Fig. 5) which excluded it from the regular galaxy classification.

Following the Rodrigues et al. (2016) methodology, given the position of PA_{kin}/PA_{phot}, dispersion map and morphology, G557 can morpho-kinematically be classified as Pec/CK, that is, peculiar morphology with a complex kinematics with two or more kinematic axes (see Fig. 3).

3.5 *HST* imaging and emission line ratio

Fig. 6 shows the integrated flux distribution maps for the narrow lines detected in the G557. The emission peak is shown with blue squares whose sizes indicate the size of the spaxel where the line was detected. The peaks of the narrow H α_{narrow} and [N II] lines are detected within the same spaxel shifted 0.2 arcsec with respect to the photometric centre of the Galaxy, equivalent to a distance of $\sim$ 1.56 kpc at z = 0.8672. The fact that both lines have their higher emission in the same spaxel supports the assumption made in Section 3.1 for the fitting of the lines that they originate in the same gas cloud.

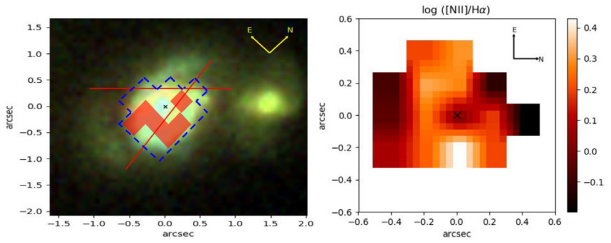

Figure 7. Left: Colour image of G557. The blue segmented lines shows the contour of the distribution map in log([N II]/H α) with the kinematic information from the [N II] emission line as described in Fig. 3. Right: [N II]/H α distribution map. Visually, it is evident that the highest log([N II]/H α) values do not coincide with the photometric centre (black cross). In addition, the zones with values greater than 0.2 are distributed in two peaks, one towards the east and the other one towards the northeast of the Galaxy. Also, the map shows values of the flux ratio associated with a composition of star formation and pure AGN activity. However, it is necessary to have IFS data from other line ratios such as log([O III]/H β) to confirm the ionization source for each region of the Galaxy.

Fig. 7 shows the distribution map of log([N II]/H α_{narrow}) for G557. Note that the maximum value of the ratio is offset from the photometric centre. In addition, areas with values greater than 0.2 are distributed in two peaks, one to the east and the other to the north-east of the Galaxy. On the other hand, we observe values of log([N II]/H α_{narrow}) that may be associated to a mix of star formation and AGN activity according to the BPT diagram. However, since we do not have access to IFU data on the log([O III]/H β) flux ratio, we cannot distinguish whether the observed log([N II]/H α_{narrow}) values are dominated by star formation in H II regions in the disc of the Galaxy or by pure AGN activity with a high ionization parameter in the Galaxy core.

To distinguish globally whether G557 corresponds to a combination between star formation and AGN, or only to pure AGN we used the integrated values of the [N II]/H α ratios from the KMOS data and the [O III]/H β ratio from the FORS2 spectrum Demarco et al. (2005).

We performed a multi-Gaussian fitting for the H $\beta\lambda$4861 line and the doublet of [O III]λ4959 and [O III]λ5007, using the PYTHON LMFIT

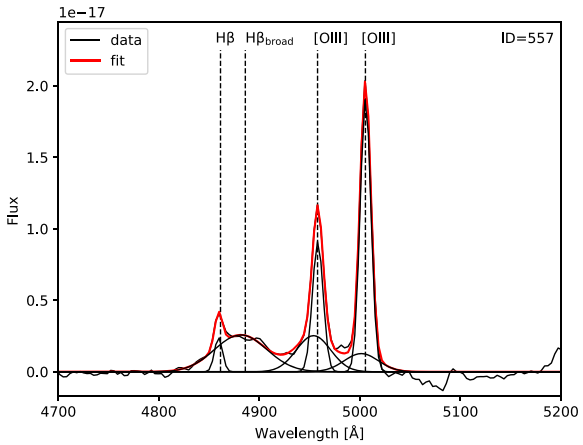

Figure 8. Integrated optical spectrum of AGN G557 in rest-frame wavelength using data from the FORS2 instrument (Demarco et al. 2005). The figure shows the best fit to the profiles of the H β line and the [O III] doublet (red curve), together with their respective Gaussian components (black curves) obtained by using PYTHON LMFIT. Similar to that found in Section 3.1 for H α, a redshifted broad component was detected for H β while for [O III] the best fit considers a blue broad component for the base of each line ('blue wing') that is associated to AGN outflows (Crenshaw et al. 2009).

package. The best fitting for FORS2 data is presented in Fig. 8. Analogous to that found for the profile of H α, the presence of a broad component was detected for H β redshifted with respect to the narrow component at a velocity of 1366 $\pm$ 166 km s^{-1} and with a FWHM = 3741 $\pm$ 339 km s^{-1}. On the other hand, for the [O III] lines, the best fit involves the presence of two components for each line, that is, a narrow one for the line centre and a broad one for the base blueshifted with respect to the line centre. These components are moving at a velocity of ~ -254 km s^{-1} and ~ -252 km s^{-1} for [O III]λ4959, and [O III]λ5007, respectively. This blueshifted base, also called 'blue wing', is associated to AGN outflows (Crenshaw et al. 2009; Woo et al. 2016; Schmidt et al. 2018).

The log([O III]/H β) flux ratio provides us with a value of 1.03, which, together with the log([N II]/H α) = 0.11 value found from the KMOS data, locate G557 within the pure AGN zone in the BPT diagram (Baldwin, Phillips & Terlevich 1981).

The emission of the broad basal component is expected to be higher for [O III]λ5007. However, the opposite is observed in the spectrum of Fig. 8 due to a loss of flux generated by telluric absorption at the longer wavelength side of the line. This telluric absorption corresponds to a line package of H_2O with a spectral range of 4964–5093 Å (Rudolf et al. 2016). Therefore, the correct measurements of the broad component and the proper flux corresponding to the narrow component cannot be assured, so the location of this Galaxy in the BPT diagram may vary vertically on the log([O III]/H β) axis from 1.03 to lower values.

4 RESULTS

4.1 AGN G557

This Galaxy corresponds to a type 1 AGN, that is, it presents narrow lines from the narrow line region (NLR) and broad lines from the BLR in the spectra obtained with KMOS and those presented by Demarco et al. (2005) using the FORS2 instrument. In both integrated spectra, a redshifted broad component from low-ionization Balmer emission lines is detected as H α with a FWHM = 4572 $\pm$ 179 km s^{-1} and a redshifted velocity of 938 $\pm$ 74 km s^{-1}, and H β with FWHM = 3741 $\pm$ 339 km s^{-1} and v = 1366 $\pm$ 166 km s^{-1}. Zhang et al. (2009) identified this same feature in a sample of AGN at redshift z < 0.37 from the SDSS DR4 (Adelman-McCarthy et al. 2006), suggesting that these objects correspond to a subclass of AGN called dbp-emitters partially obscured by the torus.

On the other hand, this Galaxy presents a clearly perturbed kinematics. This can be observed in a visual way in the maps shown in Fig. 2, and through the analysis of the dispersion peaks and kinematic axes shown in Fig. 3, where it was found that the velocity map for each emission line presents two kinematic axes that are not coincident with the photometric axis. Also, both maps have two or more peaks in velocity dispersion that are shifted with respect to the photometric centre of the Galaxy. By complementing our kinematic analysis with the morphological classification of Nantais et al. (2013), we can obtain a morpho-kinematic classification similar to that obtained for disc-galaxies by Rodrigues et al. (2016). The classification for G557 is Pec/CK, that is, a peculiar morphology with a complex kinematics with two kinematic axes. This indicates that it is a non-virialized system where a strong mismatch is observed between the distribution of the stars and the ionized gas. Comparing with other studies, the kinematical proprieties of AGN suggest the presence of non-gravitational effects such as winds that perturb the ionized gas (Riffel et al. 2013; Harrison et al. 2014, 2016; Förster Schreiber et al. 2014, 2018; Collet et al. 2016; Davies et al. 2020). Also, Collet et al. (2016) studied a sample of 18 high-redshift radio galaxies at z $\sim$ 2–3.5 finding that the kinematic properties of their sample were varied. Some galaxies showed smooth velocity gradients while others presented very disturbed velocity fields. However, none of the galaxies showed a motion of the ionized gas in a stable rotating disc which is also observed in G557.

On the other hand, analyzing the flux distribution and the log([N II]/H α) maps, we observe that the maximum value of log([N II]/H α) is not centreed as normally expected for an AGN. The map shows two peaks running relative to the photometric centre, towards the east and northeast of the Galaxy, as shown in Fig. 7. The emission distribution associated with AGN activity presents a morphology similar to the high velocity dispersion zones for [N II] that supports the idea of the presence of outflows. In addition, the map of log([N II]/H α) shows some values lower than 0.2, related, according to the BPT diagram (Groves, Heckman & Kauffmann 2006), to a composition of star-forming and AGN. To distinguish globally whether the AGN activity is dominant over the star formation, we complement the integrated value of log([N II]/H α) with the value of log([O III]/H β) measured from the optical spectrum of FORS2 Demarco et al. (2005). A multi-Gaussian fit to the emission line profile detected the presence of a narrow and a broad component for H β, while for the [O III] doublet the line profile indicates the presence of a central narrow component and a 'blue wing' (see Crenshaw et al. 2009; Woo et al. 2016; Schmidt et al. 2018). However, due to the contamination produced by telluric absorption there was a loss of flux in the red part of the line [O III]λ5007, so the broad component of it is not correctly detected. The lack of this information causes the flux measurement in each of the components of the line to be unreliable so the ratio values for log([O III]/H β) may decrease with respect to the value found in the measurement, equal to 1.03. However, because of the value log([N II]/H α) = 0.11, this Galaxy is positioned in the AGN-pure zone of the BPT diagram.

4.2 AGN G300

This Galaxy also corresponds to a type 1 AGN. However, the emission from the NLR is not observable in the spectral range of the KMOS YJ band since the narrow lines of Hα and [N II] are not distinguishable. The spectrum of this AGN only shows the broad component of Hα with a FWHM $= 3865 \pm 101$ km s^{-1}. This is also observed in low redshift AGN where, for example, Torres-Papaqui et al. (2020) found that, in a sample of 3896 Seyfert 1 (Sy1) galaxies at z < 0.4, 36 per cent of galaxies present only broad emission lines (called Sy1B). They also found differences with the Sy1 which do show narrow components (called Sy1N) reporting that the velocity of outflows are higher in the Sy1B than in the Sy1N which suggest different physical conditions in the ISM, in particular, that the Sy1N have more gas in their NLRs than the Sy1B.

For this Galaxy we performed only the morphological analysis using the fitting of elliptical isophotes presented in Section 3.3. From this analysis, it is possible to infer the presence of a bar structure that could be related to the activity of the AGN where the asymmetric potential of the bar drives the movement of the gas towards the centre of the galaxy feeding the BH (Shlosman, Frank & Begelman 1989; Sakamoto et al. 1999). However, there is no clear evidence of the influence of the bar on the internal kinematics because we cannot spatially resolve the kinematics of this AGN.

5 DISCUSSION

It is known that AGN, due to their time evolution and metal production, show super-solar metallicities (Z $>$ 2Z$\odot$; Nagao et al. 2006; Matsuoka et al. 2009), so low-metallicity AGN are very rare. Groves et al. (2006) conducted a low-metallicity AGN analysis on a sample of $\sim$23 000 Seyfert 2 galaxies at an average redshift of 0.1 in the SDSS DR4 (Adelman-McCarthy et al. 2006). They used criteria to select low-mass galaxies under the assumption of a correlation of mass and metallicity with the [N II]/Hα flux ratio. A classical example of such correlation in the local Universe can be found, e.g. in Tremonti et al. (2004). They showed that the low-metallicity AGN are characterized by a high value of log([O III]/Hβ) and a very low value of log([N II]/Hα) for the photoionization model. From that sample, only $\sim$40 galaxies correspond to AGN candidates with metallicities lower than solar that indicates the infrequency with which this type of galaxies is found at low redshift. From this, a good way to detect low-metallicity AGN is through emission line diagnostics involving the [N II]/Hα flux ratio because the relative abundance of nitrogen is proportional to the metallicity due to its nature as a secondary element (van Zee, Salzer & Haynes 1998).

Therefore, according to the flux ratio values, a metallicity of $\sim 4Z_{\odot}$ can be estimated for G557, based on its location in the BTP diagram of Fig. 2, shown in Groves et al. (2006). This indicates that this AGN is an example of high metallicity AGN.

On the other hand, this same analysis cannot be performed for G300 due to the non-detection of [N II]. The FORS2 spectrum does not show any indication of a significant [O III]λ4959,5007 emission, if any, most likely due to a poor sky subtraction and low S/N. There is no evidence for other characteristic lines of the NLR such as [O II]λ3727 and Hβ, the latter also compromised by a low S/N. We note that the dust obscuration seems unlikely to explain the lack of detection of those lines, as the FORS2 spectrum of G300 presents a blue UV continuum (Demarco et al. 2005), also supported by the photometric images shown in Fig. 5, consistent with a low obscuration level.

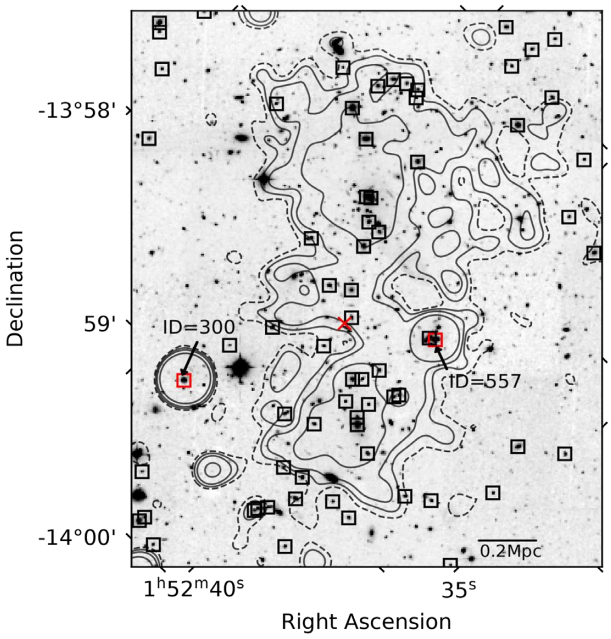

Figure 9. *HST* F850LP image of the central region of the galaxy cluster RX J0152.7–1357 at z = 0.84. The figure shows the distribution of confirmed cluster members denoted by blue squares and the position of the two AGNs in question with respect to the cluster centre (red cross) estimated by Girardi et al. (2005). We see that both AGNs are in different regions of the cluster; G557 is in the central region while G300 is on the outside. The contours correspond to X-ray emission levels 5σ, 7σ, 10σ, and 20σ above the background in the [0.5–2] keV band. FITS images provided by Demarco et al. (2005).

5.1 Environmental influence

Although both galaxies correspond to the same AGN type, we have found a significant difference in their emission lines. Then, if we considered that the lack of [N II] in G300 is an indicator of a lower metallicity in that source, is it possible that this difference in metallicity is related to the environment where these galaxies are located? As already mentioned, both galaxies are confirmed members of the cluster of galaxies RX J0152.7–1357 at z = 0.84. However, they are located in different regions of the cluster. G557 is located in the central part where there is a higher density of galaxies (Demarco et al. 2005, 2010; Jørgensen et al. 2005), gas (Maughan et al. 2003; Demarco et al. 2005, 2010), and dark matter (Jee et al. 2005). Also, this zone corresponds to the area that divides the two main sub-structures of the cluster (Demarco et al. 2005; Girardi et al. 2005), whereas G300 is located in a more outer region where the density of the cluster components decreases considerably, as shown in the Fig. 9.

Therefore, it could be argued that the difference in metallicity between these two AGN may be explained by the region of the cluster where they are located and the physical processes associated with cluster environment.

In the case of G557, which is in the innermost region near the cluster centre, their high metallicity is an indication that the Galaxy has gone already through an extended, or a short but strong, period of star formation enough to account for its metal content, which can be observed through emission lines such as [N II]. On the other hand, considering the virial radius of the cluster of $\sim$1.4 Mpc (Maughan et al. 2003) and assuming that the Galaxy falls at a speed of $\sim$250 km s^{-1} (Girardi et al. 2005), we note that this Galaxy may

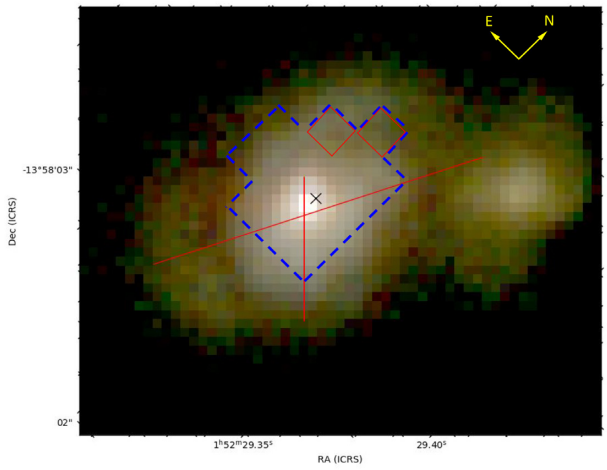

Figure 10. Colour image of G557. The blue dashed contour indicates the region where the H α narrow component was detected with the kinematic parameters described in Fig. 3 and shown here in red colour. It is evident the presence of a common envelope of stellar material surrounding the galaxies and a diffuse bridge-like substructure from one of the arms toward the nearby galaxy. Also, the velocity dispersion peaks (shown with red squares) coincide with one of the ends of the bridge which could be evidence of a possible galaxy interaction.

have taken about ∼ 3 Gyr to reach its observed position, after crossing the virial radius. If we compare with the typical lifetime of an AGN (∼ 10^5 yr; Schawinski et al. 2015), it is evident that this Galaxy suffered the activation of its BH during its fall into the cluster where some of the processes mentioned before could have accelerated its star formation and also feed its central black hole.

In addition, from the photometric images and some characteristics in the kinematic maps we can infer the possible interaction of G557 with a neighboring galaxy when observing the surface brightness flux contours in the *HST* images (see Fig. 10). A common structure between G557 and the other galaxy present in the image can be seen which may correspond to a halo of stars ripped off from both galaxies by the tidal forces during the collision process. Also, it is visible a bridge of material connecting (in projection) those objects, and whose position also coincides with the spaxels with high velocity dispersion for the H α narrow component (the red squares), as shown in Fig. 10, thus indicating a possible excitation of the ionized gas in that zone product of a merger. It is known that interactions between galaxies can lead to a loss of angular momentum of the gas in the ISM, bringing, as a consequence, material towards the galactic centre (Barnes & Hernquist 1991). In this way, it is possible to associate the interaction of G557 with its nearby galaxy as one of the processes responsible for the activation of its central black hole. However, this interpretation needs more data in order to confirm that this other galaxy is a member of the cluster. In fact, no redshift for this secondary, possibly interacting, galaxy has been previously reported in the literature (Jørgensen et al. 2005; Demarco et al. 2005, 2010).

On the other hand, G300's morphology, its broad-line emission spectrum, and its location in the clusters suggest that the cluster environment is not playing a major role in its observed properties. It is located in an area with a lower local environmental density as shown by both the dark matter mass distribution, the distribution of galaxies, and ICM gas. Its AGN is likely powered by the action of its bar, and the lack of narrow emission features is indicative of a galaxy devoid of current star formation, possibly the consequence of pre-processing before incorporation into the cluster environment. Mergers are not common in the outskirts of clusters as galaxies move fast, and the regular morphology of G300 is inconsistent with any recent merger event.

6 SUMMARY AND CONCLUSIONS

The technique of integral field spectroscopy in the near-infrared with KMOS at the *VLT* allowed us to spatially resolve the kinematics of one AGN member of the cluster RX J0152.7–1357 at z = 0.84. This was done by performing a multi-Gaussian fitting to the emission line profiles that enabled the subsequent construction of the velocity and velocity dispersion maps. By combining the kinematic and photometric analysis with previous information on this Galaxy, we are able to obtain a more complete view of the properties of this AGN through a morpho-kinematic classification. Also, we compare it with other AGN of the same galaxy cluster to identify differences that may be related to the cluster environment in which they develop.

In summary, the main results of this investigation are:

(i) Both AGN have a rest-frame optical spectrum with characteristics of type 1 AGN.

(ii) The integrated spectrum of G557 presents a broad component redshifted with respect to the narrow component for Balmer emission lines. This could be evidence that this AGN corresponds to a type of AGN called dbp-emitters, which would be partially obscured by the torus according to Zhang et al. (2009).

(iii) G557 can be classified morpho-kinetically as Pec/CK, i.e. a galaxy with peculiar morphology with complex kinematics. The kinematic analysis shows the presence of more than one kinematic axis and several velocity dispersion peaks that suggest that this Galaxy corresponds to a non-virialized system. This indicates a possible previous event such as a merger or other interaction.

(iv) The G557 show evidence of a radial outflow that is supported by the detection of the 'blue wings' in the [O III] emission from the FORS2 spectrum.

(v) The values of log([N II]/H α) = 0.11 and log([O III]/H β) = 1.03 place the G557 in the AGN-pure zone of the BPT diagram. However, the value of log([O III]/H β) is not certain due to the loss of flux caused by telluric absorption in the FORS2 spectrum.

(vi) For G300, the non-detection of narrow emission lines and its morphology suggest that this Galaxy may correspond to a subclass of Seyfert 1 galaxy classified as Sy1B by Torres-Papaqui et al. (2020).

(vii) Based on what it is proposed by Groves et al. (2006) about the relation between metallicity and the [N II] emission line strength, we found that G557 corresponds to a high metallicity AGN with a value of Z ∼ $4Z_{\odot}$, while the G300 could correspond to an example of a low metallicity AGN at high redshift due to the lack of [N II] emission and the non-significant detection of [O II] and [O III] emission lines on the FORS2 spectrum. However, this hypothesis requires to be confirmed with more observations that allow for a proper analysis of the metallicity of this Galaxy. We note that the lack of detection, even though it could be due to a low S/N near the H β and [O III] lines, is unlikely to be due to internal dust obscuration.

ACKNOWLEDGEMENTS

We acknowledge support by Comisión Nacional de Investigación Científica y Tecnológica (CONICYT) Programa de Astronomía

Fondo ALMA-CONICYT 2017 31170002. RD gratefully acknowledges support from the Chilean Centro de Excelencia en Astrofísica y Tecnologías Afines (CATA) BASAL grant AFB-17000. YJ acknowledges financial support from CONICYT PAI (Concurso Nacional de Inserción en la Academia 2017) No. 79170132, and Fondo Nacional de Desarollo Científico y Tecnológico (FONDECYT) Iniciación 2018 No. 11180558. JN received support from Universidad Andres Bello internal grant DI-12-19/R.

DATA AVAILABILITY

The data underlying this article will be shared on reasonable request to the corresponding author. The raw data can be download directly from the ESO SCIENCE ARCHIVE FACILITY platform (https://archive.eso.org/eso/eso_archive_main.html) using the following program IDs: 092.A-0868, 093.A-0834, 096.A-0171, and 098.A-0380.

REFERENCES

Adelman-McCarthy J. K. et al., 2006, ApJS, 162, 38
Aird J., Coil A. L., Georgakakis A., Nandra K., Barro G., Pérez-González P. G., 2015, MNRAS, 451, 1892
Alexander D. M., Hickox R. C., 2012, NAR, 56, 93
Astropy Collaboration, 2013, A&A, 558, A33
Astropy Collaboration, 2018, AJ, 156, 123
Bacon R. et al., 2010, in McLean I. S., Ramsay S. K., Takami H., eds, Proc. SPIE Conf. Ser. Vol. 7735, Ground-based and Airborne Instrumentation for Astronomy III. SPIE, Bellingham. p. 773508
Baldwin J. A., Phillips M. M., Terlevich R., 1981, PASP, 93, 5
Barazza F. D., Jogee S., Marinova I., 2008, ApJ, 675, 1194
Barnes J. E., Hernquist L. E., 1991, ApJ, 370, L65
Bassett R. et al., 2013, ApJ, 770, 58
Blakeslee J. P. et al., 2006, ApJ, 644, 30
Bufanda E. et al., 2016, MNRAS, 465, 2531
Butcher H., Oemler A. J., 1984, ApJ, 285, 426
Collet C. et al., 2016, A&A, 586, A152
Combes F., Sanders R. H., 1981, A&A, 96, 164
Cowie L. L., Songaila A., 1977, Nature, 266, 501
Crenshaw D. M., Schmitt H. R., Kraemer S. B., Mushotzky R. F., Dunn J. P., 2009, ApJ, 708, 419
Davies R. I., 2007, MNRAS, 375, 1099
Davies R. I. et al. 2013, A&A, 558, A56
Davies R. L. et al. 2019, ApJ, 873, 122
Davies R. L. et al. 2020, ApJ, 894, 28
Delgado-Serrano R., Hammer F., Yang Y. B., Puech M., Flores H., Rodrigues M., 2010, A&A, 509, A78
Demarco R. et al., 2005, A&A, 432, 381
Demarco R. et al. 2010, ApJ, 725, 1252
Donoso E., Yan L., Stern D., Assef R. J., 2014, ApJ, 789, 44
Dressler A., 1980, ApJ, 236, 351
Dressler A., Thompson I. B., Shectman S. A., 1985, ApJ, 288, 481
Ehlert S. et al., 2014, MNRAS, 437, 1942
Eisenhauer F. et al. 2003, in Iye M., Moorwood A. F. M., eds, Proc. SPIE Conf. Ser. Vol. 4841, Instrument Design and Performance for Optical/Infrared Ground-based Telescopes. SPIE, Bellingham, p. 1548
Ellingson E., Lin H., Yee H. K. C., Carlberg R. G., 2001, ApJ, 547, 609
Fabian A., 2012, ARAA, 50, 455
Farouki R., Shapiro S. L., 1981, ApJ, 243, 32
Flores H., Hammer F., Puech M., Amram P., Balkowski C., 2006, A&A, 455, 107
Förster Schreiber N. M. et al. 2006, ApJ, 645, 1062
Förster Schreiber N. M. et al. 2009, ApJ, 706, 1364
Förster Schreiber N. M. et al. 2014, ApJ, 787, 38
Förster Schreiber N. M. et al., 2018, ApJS, 238, 21
Franceschini A., Hasinger G., Miyaji T., Malquori D., 1999, MNRAS, 310, L5
Galametz A. et al. 2009, ApJ, 694, 1309
Genzel R. et al. 2006, Nature, 442, 786
Girardi M., Demarco R., Rosati P., Borgani S., 2005, A&A, 442, 29
Gnedin O. Y., 2003, ApJ, 582, 141
Gravity Collaboration, 2020a, A&A, 634, A1
Gravity Collaboration, 2020b, A&A, 643, A154
Groves B., Heckman T., Kauffmann G., 2006, MNRAS, 371, 1559
Gunn J. E., Gott J. R., III, 1972, ApJ, 176, 1
Harrison C. M., Alexander D. M., Mullaney J. R., Swinbank A. M., 2014, MNRAS, 441, 3306
Harrison C. M. et al. 2016, MNRAS, 456, 1195
Harrison C. M. et al. 2017, MNRAS, 467, 1965
Holden B. P. et al. 2007, ApJ, 670, 190
Hopkins P. F., Hernquist L., Cox T. J., Di Matteo T., Robertson B., Springel V., 2006, ApJS, 163, 1
Hopkins P. F., Hernquist L., Cox T. J., Kereš D., 2008, ApJS, 175, 356
Houghton R. C. W., 2015, MNRAS, 451, 3427
Jee M. J., White R. L., Benítez N., Ford H. C., Blakeslee J. P., Rosati P., Demarco R., Illingworth G. D., 2005, ApJ, 618, 46
Jones T., Ellis R. S., Richard J., Jullo E., 2013, ApJ, 765, 48
Jørgensen I., Bergmann M., Davies R., Barr J., Takamiya M., Crampton D., 2005, ApJ, 129, 1249
Kauffmann G. et al. 2003, MNRAS, 346, 1055
Kormendy J., Ho L. C., 2013, ARAA, 51, 511
Larkin J. et al. 2006, New Astron. Rev., 50, 362
Larson R. B., Tinsley B. M., Caldwell C. N., 1980, ApJ, 237, 692
Madau P., Dickinson M., 2014, ARAA, 52, 415
Marinova I., Jogee S., 2007, ApJ, 659, 1176
Martini P. et al. 2013, ApJ, 768, 1
Matsuoka K., Nagao T., Maiolino R., Marconi A., Taniguchi Y., 2009, A&A, 503, 721
Maughan B. J., Jones L. R., Ebeling H., Perlman E., Rosati P., Frye C., Mullis C. R., 2003, ApJ, 587, 589
Mei S. et al., 2012, ApJ, 754, 141
Merloni A., Rudnick G., Di Matteo T., 2004, MNRAS, 354, L37
Merritt D., 1983, ApJ, 264, 24
Moore B., Katz N., Lake G., Dressler A., Oemler A., 1996, Nature, 379, 613
Nagao T., Maiolino R., Marconi A., 2006, A&A, 447, 863
Nantais J. B., Flores H., Demarco R., Lidman C., Rosati P., Jee M. J., 2013, A&A, 555, A5
Neichel B. et al. 2008, A&A, 484, 159
Osterbrock D., Ferland G., 2006, The Astrophysics of Gaseous Nebulae and Active Galactic Nuclei. University Science Books, Sausalito California
Overzier R. A., 2016, A&AR, 24 14
Peng C. Y., Ho L. C., Impey C. D., Rix H.-W., 2002, ApJ, 124, 266
Pentericci L. et al., 2013, A&A, 552, A111
Petersen M. S., Weinberg M. D., Katz N., 2019, MNRAS, 490, 3616
Peterson B. M., 1997, An Introduction to Active Galactic Nuclei. Cambridge Univ. Press, Cambridge
Poggianti B. M. et al. 2017, ApJ, 844, 48
Postman M., Geller M. J., 1984, ApJ, 281, 95
Postman M. et al. 2005, ApJ, 623, 721
Radovich M., Poggianti B., Jaffé Y. L., Moretti A., Bettoni D., Gullieuszik M., Vulcani B., Fritz J., 2019, MNRAS, 486, 486
Rettura A. et al. 2011, ApJ, 732, 94
Richstone D. O., 1976, ApJ, 204, 642
Riffel R. A., Storchi-Bergmann T., Winge C., 2013, MNRAS, 430, 2249
Rodrigues M., Hammer F., Flores H., Puech M., Athanassoula E., 2016, MNRAS, 465, 1157
Rudolf N., Günther H. M., Schneider P. C., Schmitt J. H. M. M., 2016, A&A, 585, A113
Sakamoto K., Okumura S. K., Ishizuki S., Scoville N. Z., 1999, ApJ, 525, 691
Schawinski K., Koss M., Berney S., Sartori L. F., 2015, MNRAS, 237, 692

Schmidt E. O., Oio G. A., Ferreiro D., Vega L., Weidmann W., 2018, A&A, 615, A13
Shapiro K. L. et al. 2008, ApJ, 682, 231
Sharples R. et al. 2004, in Moorwood A. F. M., Masanori I., eds, Proc. SPIE Conf. Ser., Ground-based Instrumentation for Astronomy. SPIE, Bellingham, p. 5492
Sharples R. et al. 2013, Messenger, 151, 21
Sheen Y.-K. et al. 2017, ApJL, 840, L7
Sheth K., Regan M. W., Scoville N. Z., Strubbe L. E., 2003, ApJL, 592, L13
Shlosman I., Frank J., Begelman M. B., 1989, Nature, 338, 45
Somerville R. S., Davé R., 2015, ARAA, 53, 51
Stott J. P. et al. 2016, MNRAS, 457, 1888
Torres-Papaqui J. P. et al. 2020, ApJ, 160, 176
Treister E., Natarajan P., Sanders D. B., Urry C. M., Schawinski K., Kartaltepe J., 2010, Science, 328, 600
Treister E., Schawinski K., Urry C. M., Simmons B. D., 2012, ApJ, 758, L39
Tremonti C. A. et al. 2004, ApJ, 613, 898
van der Wel A. et al. 2007, ApJ, 670, 206
van Zee L., Salzer J. J., Haynes M. P., 1998, ApJL, 497, L1
Weinberg M. D., 1985, MNRAS, 213, 451
Weinberg M. D., Katz N., 2007, MNRAS, 375, 460
Wisnioski E. et al. 2015, ApJ, 799, 209
Wisnioski E. et al. 2019, ApJ, 886, 124
Woo J.-H., Bae H.-J., Son D., Karouzos M., 2016, ApJ, 817, 108
Yang Y. et al., 2008, A&A, 477, 789
Zhang X.-G., Deborah D., Ting-Gui W., Guinevere K., 2009, MNRAS, 397, 1510

This paper has been typeset from a TEX/LATEX file prepared by the author.